### Title

Single Small Molecule-Assembled Mitochondria Targeting Nanofibers for Enhanced Photodynamic Cancer Therapy In Vivo




### Journal

Advanced Functional Materials, 31(10)

### ISSN

1616-301X



### Authors

Lin, Kai
Ma, Zhao
Li, Jin
et al.



### Publication Date

2021-03-01

### DOI

10.1002/adfm.202008460

Peer reviewed

Published in final edited form as:

*Adv Funct Mater*. 2021 March 03; 31(10): . doi:10.1002/adfm.202008460.

# Single Small Molecule-Assembled Mitochondria Targeting Nanofibers for Enhanced Photodynamic Cancer Therapy in Vivo

**Kai Lin**[§],
Department of Biochemistry and Molecular Medicine, UC Davis Comprehensive Cancer Center, University of California Davis, Sacramento, CA 95817, USA

Department of Urology and Pathology, New York University School of Medicine, New York, NY 10016, USA

**Zhao Ma**[§],
Department of Biochemistry and Molecular Medicine, UC Davis Comprehensive Cancer Center, University of California Davis, Sacramento, CA 95817, USA

**Jin Li**,
Department of Biochemistry and Molecular Medicine, UC Davis Comprehensive Cancer Center, University of California Davis, Sacramento, CA 95817, USA

**Menghuan Tang**,
Department of Biochemistry and Molecular Medicine, UC Davis Comprehensive Cancer Center, University of California Davis, Sacramento, CA 95817, USA

**Aaron Lindstrom**,
Department of Biochemistry and Molecular Medicine, UC Davis Comprehensive Cancer Center, University of California Davis, Sacramento, CA 95817, USA

**Mythili Ramachandran**,
Department of Biochemistry and Molecular Medicine, UC Davis Comprehensive Cancer Center, University of California Davis, Sacramento, CA 95817, USA

**Shaoming Zhu**,
Department of Internal Medicine, University of California Davis, Sacramento, CA 95817, USA

**Tzu-yin Lin**,
Department of Internal Medicine, University of California Davis, Sacramento, CA 95817, USA

**Lanwei Zhang**,
School of Chemistry and Chemical Engineering, Harbin Institute of Technology, Harbin 150000, China

mzma@ucdavis.edu, lypli@ucdavis.edu.
[§]These authors contributed equally to this work.

Supporting Information

Supporting Information is available from the Wiley Online Library or from the author.

Conflict of Interest

Y. Li and Z. Ma are the co-inventors on a pending patent application on the mitochondria targeting compounds and the resulting nanoformulations. The remaining authors declare no competing interests.

**Yuanpei Li**
Department of Biochemistry and Molecular Medicine, UC Davis Comprehensive Cancer Center, University of California Davis, Sacramento, CA 95817, USA

## Abstract

Photodynamic therapy (PDT) has emerged as an attractive alternative in cancer therapy, but its therapeutic effects are limited by the nonselective subcellular localization and poor intratumoral retention of small-molecule photosensitizes. Here a fiber-forming nanophotosensitizer (PQC NF) that is composed of mitochondria targeting small molecules of amphiphilicity is reported. Harnessing the specific mitochondria targeting, the light-activated PQC NFs produce approximately 110-fold higher amount of reactive oxygen species (ROS) in cells than free photosensitizers and can dramatically induce mitochondrial disruption to trigger intense apoptosis, showing 20–50 times better *in vitro* anticancer potency than traditional photosensitizers. As fiber-shaped nanomaterials, PQC NFs also demonstrated a long-term retention in tumor sites, solving the challenge of rapid clearance of small-molecule photosensitizers from tumors. With these advantages, PQC NFs achieve a 100% complete cure rate in both subcutaneous and orthotopic oral cancer models with the administration of only a single dose. This type of single small molecule-assembled mitochondria targeting nanofibers offer an advantageous strategy to improve the *in vivo* therapeutic effects of conventional PDT.

## Abstract

An amiphiphilic photosensitizer-derived small molecule that can self-assemble into a fiber-forming nanoconstruct was developed. The one-component nanofiber not only exhibits a significantly phototoxicity to cancer cells through targeting mitochondria, but also shows the long-term retention in tumor site, thus achieving a 100% complete cure rate in both subcutaneous and orthotopic oral cancer models with only a single-dose administration.

## Graphical Abstract

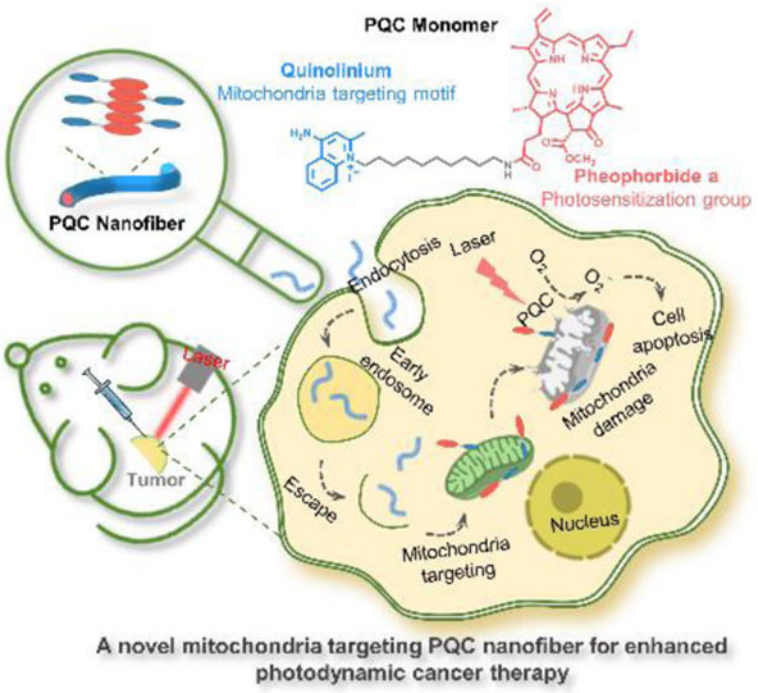


**Keywords**

self-assembly; nanofiber; small-molecule drug conjugate; mitochondria targeting; photodynamic therapy

## 1. Introduction

Photodynamic therapy (PDT) is a well-established clinical treatment modality for cancer, which combines the photosensitizer, light energy, and oxygen to produce singlet oxygen ($^1O_2$) and trigger a chain of reactions of reactive oxygen species (ROS) leading to cell death.[1] The technique is gaining popularity due to its minimally invasive nature for patients, short-course treatment, and selective cytotoxicity.[2] Since $^1O_2$ has a short lifetime (~3 μs) and a limited diffusion radius (0.02 μm), the photosensitizer only causes photodamage in its direct vicinity. Therefore, the efficiency of PDT is strongly dependent on the intracellular accumulation and subcellular localization of photosensitizers.[3] To address this challenge, a promising solution is delivering the photosensitizers to specific organelles, where $^1O_2$ is generated *in situ* to efficiently trigger phototoxicity.[4] As the main powerhouse and important ROS source in cells, the mitochondrion is a potentially excellent target for PDT.[5] Since the inner mitochondrial membrane has a strong negative membrane potential, mitochondria targeting PDT can be achieved by conjugating photosensitizers to delocalized cations, such as triphenylphosphonium (TPP) and dequalinium (DQA).[6] Several reported mitochondria-targeted photosensitizers have shown significantly improved therapeutic effects relative to their free photosensitizer.[7]

Another limitation for traditional PDT is the rapid clearance of the small-molecule photosensitizers from tumors, which causes the poor retention of photosensitizers in tumor cells and insufficient therapeutic effects *in vivo*.[8] Self-assembling nanomaterials are retained longer at local sites, which gives the potential to overcome this limitation of photosensitizer clearance.[9] Through supramolecular self-assembly, small-molecule drugs can be functionalized with superior nanoscale characteristics and self-delivering properties.[10] This carrier-free nanomedicine strategy urges the development of small-molecule nanophotosensitizers.[11] However, most of the developed nanophotosensitizers are spherical nanoparticles, not nanofibers. Compared to the traditional spherical nanoparticles, the fiber-forming nanomedicines are revolutionizing the field of drug delivery due to their high surface-area-to-volume ratio, small inter-fibrous pore size with high porosity, and enhanced retention effects.[12] Among the attempts to construct nanofibers, the majority of building blocks are β-sheet peptide-based motifs that are utilized to drive supramolecular assembly and hydrogel formation.[13] Although these peptide assemblies have demonstrated great advantages of nanofibers in medical diagnosis and therapy, there remain practical and system-specific challenges in the manufacture of peptide materials and complex self-assembly process.[14] Since these limitations can be overcome by small-molecule drugs, recently small molecule-based nanofibers have drawn attention. However, due to the lack of available fiber-forming small-molecule monomers, there are only limited reported cases to date.[15]

Herein, according to the above strategies to improve PDT and principles of new drug design and molecular self-assembly, we developed a mitochondria-targeting nanofiber (PQC NF) that are formed by self-assembly of small-molecule building blocks of amphiphilicity (Figure 1) for the photodynamic cancer therapy. The monomer is a pheophorbide a (PA) and quinolinium conjugate (PQC), in which the hydrophobic PA acts as the photosensitization group and the quinolinium moiety is hydrophilic cation for mitochondria targeting.[16] PQC NFs could specifically accumulate in mitochondria and are retained there for an extended period, where they exhibited a powerful PDT effect to induce mitochondrial disruption and lead to apoptotic cell death. When compared with free PA, PQC NFs showed a 20–50-fold increase in cytotoxicity *in vitro* and can be retained within tumor sites *in vivo* for 10 days. Using these advantages, PQC NFs achieved a powerful tumor ablation effect in both subcutaneous and orthotopic oral cancer models when treated with only a single dose. As fiber-shaped nanophotosensitizers that are self-assembled from mitochondria-targeted small molecules, PQC NFs provide a useful strategy to chemically modify existing photosensitizers to enhance their phototherapeutic effects.

## 2. Result and Discussion

### 2.1. Synthesis and Characterization of PQC Monomer

The PQC monomer was synthesized by conjugating PA with 4-aminoquinaldine through a 1-decanamine linker (Figure S1, Supporting Information). All intermediates and the target compound were chemically characterized by nuclear magnetic resonance (NMR) spectroscopy and electrospray-ionization mass spectrometry (MS) (Figure S2-S5, Supporting Information). The UV-visible and fluorescence spectra were also used for

structure confirmation (Figure 2a). Together with the PA and PQC molecules, DQA, was also employed as the control. Free PQC molecules showed three main absorption peaks, with one at ~350 nm from the absorbance of quinolinium moiety and the other two at 412 nm and 675 nm from the absorbance of PA (Figure 2b). In terms of fluorescence, the PQC molecules exhibited similar emission spectra to PA in methanol (Figure 2c).

## 2.2. Construction and Characterization of PQC NFs

The self-assembling PQC NFs were prepared via a nanoprecipitation method, in which the PQC solution in ethanol was added into water dropwise, followed by the evaporation of ethanol under reduced pressure. By using transmission electron microscopy (TEM), we found that PQC molecules self-assembled into the uniform nanofiber scaffold networks with average diameters of 14.9±2.5 nm and a surface charge of 42.3±1.3 mV (Figure 2d). The positive surface charge comes from the cationic quinolinium, indicating that quinolinium moieties spread over the surface of PQC NFs. The critical aggregation concentration (CAC) of PQC NFs was measured to be 0.085 μg $mL^{-1}$ (Figure S6, Supporting information).[17] The ultrafiltration method was then employed to identify the formation of PQC NFs (Figure 2e). The majority of PQC NFs were retained in the centrifugal filter (10 kDa), showing a dark green color and strong fluorescence, while the colorless filtrate with low fluorescence indicated only a trace amount of PQC molecules.

The morphological structure of amphiphilic self-assembled aggregates depends on the relative size of the hydrophobic and hydrophilic moieties.[18] In the PQC molecule, there are a large hydrophobic PA group (mw=590) and a small hydrophilic quinolinium group (mw=158). This high hydrophobicity-to-hydrophilicity ratio determines the aggregation of PQC molecules into nanofibers. The formation of aggregates also benefits from the strong π-π stacking interactions among PA moieties of PQC molecules.[19] MS was employed to explore the structure of PQC aggregates in aqueous conditions, which is a powerful tool to investigate the assembly of small molecules.[20] The PQC monomers (m/z 888.517), dimers (m/z 1777.034), tetramers (m/z/4 1184.689) and heptamers (m/z/6 1036.603) were observed from MS (Figure S7, Supporting information), suggesting that the PQC molecule is the building block that aggregates into nanofibers. DQA, the control, which has been demonstrated to self-assemble into liposome-like vesicles (DQAsomes), was also included in this study.[21] As the interactions of hydrophobic chains are very weak, DQA did not show any signals of multimer in the MS spectra (Figure S7, Supporting information).

Without a bio-cleavable chemical bond in its chemical structure, the PQC monomer is not a prodrug form of an existing photosensitizer, but a new chemical entity that possesses an excellent self-assembling property. Therefore, compared to the majority of traditional nanoformulations that are prepared by physical loading or prodrug self-assembly of existing drugs, the new-chemical-entity-assembled PQC NFs represent a structure innovation in the perspective of new drug discovery. Additionally, the one-component PQC NFs have a 100% drug loading efficiency and show enormous advantages to break through the drug-loading and scale-up production limitations of the conventional drug delivery systems.[22]

### 2.3 Optical Property and ROS Production in Solutions

It is known that the PA fluorophore has an aggregation caused quenching (ACQ) effect on its fluorescence emission.[23] Upon the self-assembly, the aggregated PA moieties localized inside the PQC NFs and showed a very weak fluorescence emission (Figure 2f). After dissociation by sodium dodecyl sulfate (SDS), their fluorescence was recovered. The aggregation-dissociation-based fluorescence “off-on” behavior was also observed with near-infrared (NIR) fluorescence imaging (Figure 2g). The PQC NFs in PBS showed low fluorescence due to the ACQ effect, and when dissociated in PBS/SDS, they exhibited a concentration-dependent fluorescence enhancement as expected. The hydrophobic PA compound also showed a similar ACQ behavior as PQC NFs, indicating PA was aggregated as well in PBS. However, because the carboxylic acid group is not an excellent hydrophilic moiety, the aggregates of PA displayed a scattered size distribution from nanometers to micrometers and a negative surface charge of −11.5 ± 1.3 mV (Figure S8, Supporting information). As the pioneering theranostic agents, porphyrin derivatives can be used for both photodynamic therapy and NIR fluorescence imaging.[24] This “off-on” fluorescent property can be used to track the permeability and persistence of PQC nanofibers in tumor sites specifically.

When absorbing a specific wavelength of light, photosensitizers can convert oxygen into $^1O_2$, which consequently causes an increase of ROS and is a critical anticancer mechanism of PDT.[25] Moreover, for a photosensitization group, the singlet oxygen quantum yield is an intrinsic property, and modifying the photosensitizer by conjugation with other moieties may cause the decrease of singlet oxygen production efficacy in solution.[6a] Singlet oxygen sensor green (SOSG) was used as a probe to determine the $^1O_2$ production induced by PA and PQC NFs in solutions. As shown in Figure 2h, PQC NFs produced a similar amount of $^1O_2$ with PA at the same concentration, which indicates that chemical conjugation did not impede the ability of $^1O_2$ production. In addition, both PQC NFs and PA produced limited $^1O_2$ in the aggregation forms (in PBS), while their dissociated forms (in PBS/SDS) showed an increased capacity of $^1O_2$ production (Figure 2h), indicating the $^1O_2$ production can be specifically activated by their free molecules, rather than their aggregates. These results are consistent with our aforementioned findings of the fluorescence “off-on” behavior of PQC NFs, which allows for specific photodynamic reactions for use as highly selective cancer therapies.[26]

### 2.4. In Vitro Anticancer Activity

After characterizing the properties and functions of PQC NFs in solutions, we moved to evaluate the *in vitro* anticancer effects in cells. The OSC-3 cell line, a type of superficial oral squamous cell carcinoma, was chosen firstly because PDT is ideally suited to this cancer type and some related therapies have already been approved by FDA for use in the clinic.[27] The viability of OSC-3 cells was measure using the CellTiter-Glo cell viability assay (Figure 3a). In the absence of light, PA did not show cytotoxicity even at 100 uM, while PQC NFs showed similar cytotoxicity with DQA and the mixed treatment ($IC_{50}$=3 μM). When cells were exposed to light treatment, PQC NFs showed a dramatically increased anticancer effect against OSC-3 cells ($IC_{50}$=0.12 μM), which is 10-fold and 21-fold more potent than that of the mixed treatment ($IC_{50}$=1.21 μM) or PA ($IC_{50}$=2.57 μM), respectively. Remarkably, the

control groups of DQA, PA, and their mixture did not show obvious anticancer effects at the concentration range from 0.3 μM to 1 μM, while PQC NFs eliminated all the OSC-3 cancer cells at those concentrations. Moreover, PQC NFs were superior to other nanoformulations of PA, such as PA-loaded liposomes (liposomes@PA) and PA-conjugated polymers ($PEG^{5k}$-$PA_4$-$CA_4$) (Figure S9, Supporting Information).[23] These cytotoxicity findings strongly support our hypothesis that delivering photosensitizers into mitochondria can greatly improve their therapeutic effects. In the extended cell viability assays (Figure S10, Supporting information), it was also found that the light-treated PQC NFs had 32 to 48 times higher potency than light-treated PA in inhibiting pancreatic cancer cells (BXPC-3, AsPC-1, and PANC-1) and bladder cancer cells (UM-UC-3 and 5637), implying their considerable potential to be applied to other cancer types. Compared to these cancer cells, the noncancerous IMR90 cells were more tolerated to PQC NFs in both the absence and presence of light irradiation, which suggests that PQC NFs have relatively low toxicity to the noncancerous cell line (Figure S10, Supporting information).

### 2.5 Cellular Uptake and Endocytosis

To illuminate the intracellular characteristics of PQC NFs, a cellular uptake study was conducted (Figure 3b and Figure S11, Supporting information). PQC NFs showed a time-dependent accumulation in OSC-3 cells and achieved a significantly improved profile of cellular uptake than free PA. This is attributable to the effective self-assembling properties of PQC NFs, including their homogeneous nanosize characteristics and positive surface charge.[28] To interrogate the endocytosis mechanism of PQC NFs, the entry of PQC NFs into cells was measured when incubation was performed at low temperature. The results show the decrease in temperature inhibited cellular uptake of PQC NFs, which suggests the endocytosis PQC NFs is energy-dependent (Figure 3c and Figure S12, Supporting information).[29] Four types of endocytosis inhibitors were then utilized to reveal the specific endocytic pathway of PQC NFs: sodium azide, chlorpromazine, genistein, and amiloride. Among these, both sodium azide and chlorpromazine decreased the cellular uptake of PQC NFs, which implicated that PQC NFs entered cells mainly through clathrin-mediated endocytosis, rather than caveolae-mediated endocytosis (genistein) or micropinocytosis (amiloride) (Figure 3d and Figure S12, Supporting information).[30]

### 2.6 Mitochondrial Targeting

We subsequently investigated the subcellular localization of PQC NFs by using confocal microscopy. OSC-3 cells were incubated with PQC NFs for different time points (from 5 min to 8 h), followed by staining cells with MitoTracker and LysoTracker before imaging. As depicted in Figure 3e, PQC NFs (red) and mitochondria (green) colocalized quickly (within 5 min) as indicated by the yellow color on the merged overlay. The calculated Pearson correlation coefficients in Figure 3f indicate a high degree of colocalization between PQC NFs and mitochondria at 5 min (Pearson's R, 0.72), and the colocalization reached the maximum in 2 h (Pearson's R, 0.87). However, the colocalization with lysosomes was only moderate at 5 min (Pearson's R, 0.43) and decreased in a time-dependent manner. These results demonstrate that PQC NFs can quickly enter the mitochondria of living cells and remain there for hours. In contrast, the parental PA molecules were diffused into the cytoplasm and exhibited a low-level colocalization with mitochondria or lysosomes,

indicating an obvious difference with the mitochondria-targeted subcellular distribution of PQC NFs (Figure 3g). We also isolated the mitochondria and cytoplasm of OSC-3 cells following a 24 h pretreatment with PQC NFs or PA to quantify the differences in their localization. The PQC concentration in mitochondria was 24-fold higher than that in the cytoplasm, while PA molecules showed a similar concentration in both mitochondria and cytoplasm, confirming that PQC NFs are specifically targeted to mitochondria (Figure 3h).

### 2.7 Intracellular Dissociation

We next investigated the intracellular dissociation behavior of PQC NFs, in which PQC NFs (100 μM) were incubated with the freshly isolated mitochondria (0.1 mg $mL^{-1}$), lysosomes (0.1 mg $mL^{-1}$), and other cellular components (0.1 mg $mL^{-1}$) for 24 h and were then observed by TEM (Figure S13, Supporting information). It was found that PQC NFs stayed in the aggregation state upon incubation with the lysosomal or cellular component that did not contain mitochondria, but were dissociated in presence of the mitochondria component. This is because the mitochondria inner membrane with strongly negative potential can bind to the delocalized cationic quinolinium moiety on the surface of PQC NFs, which drives the dissociation of NFs into free molecules. Based on these findings, we can conclude that PQC NFs maintained their nanostructures in the process of cell endocytosis and intracellular transport toward mitochondria, and then were dissociated into free molecules in mitochondria. Since the free form of PQC NFs can produce more ROS than the aggregation form (Figure 2h), the dissociation of PQC NFs that selectively occurs in mitochondria can be conducive to improve the efficiency of PDT.

### 2.8 Intracellular ROS Production

As ROS overproduction is the key anticancer mechanism of PDT, we measured the ROS levels in OSC-3 cancer cells treated with PQC NFs by using 2',7'-dichlorofluorescein diacetate (DCF-DA) as a fluorescence sensor.[31] After exposure to light, PQC NFs produced approximately 110-fold higher amounts of ROS than the same concentration of free PA (Figure 4a). Because the PQC NFs and PA have a similar $^1O_2$ quantum yield, and the intracellular concentration of PQC NFs is only 1.4 times as that of PA (Figure 2h and 3b), this significant enhancement of intracellular ROS production should be attributable to their specific mitochondria targeting property of PQC NFs. As mitochondria are an important source of ROS in most mammalian cells, mitochondria-targeted PQC NFs potentially caused ROS burst *in situ* through mitochondrial imbalance.[32]

### 2.9. Mitochondrial Disruption

To get direct insights in PQC NF-mediated mitochondrial damage, the mitochondrial membrane potential was determined using indicator dye JC-1. JC-1 forms J-aggregates in cells with high mitochondrial membrane potential and emits red fluorescence, while it remains monomeric in cells with low mitochondrial membrane potential and emits green fluorescence.[33] Representative results from PQC NFs treatment of OSC-3 cells are displayed in Figure 4b. No differences were observed among the groups without light treatment, indicating the relatively low dark toxicity of PQC NFs toward mitochondria. Remarkably, the simultaneous treatment of cells with PQC NFs (1 μM) and light caused a decline of red fluorescence signals and the rise of green fluorescence signals, which

indicates a severe loss of mitochondrial membrane potential. In contrast, the control treatments with PA or DQA upon light illumination were not effective enough to cause a signal change at the same condition of 1 μM. Treatment with a higher concentration of PA (4 μM), the positive control, was milder when compared to 1 μM PQC NFs as those treated cells still exhibited red fluorescence (Figure S14, Supporting information). To confirm the visual results, the calculated red-to-green fluorescence ratio of cells in each treatment further showed the potent ability of PQC NFs to induce mitochondria depolarization (Figure 4c).

We next used TEM to investigate the morphological changes in mitochondria induced by PQC NFs treatment. As shown in Figure 4d, the vehicle or PA-treated cells without light that showed healthy mitochondria with typical tubular cristae and crista junctions in the absence of light, while DQA-treated cells displayed morphologically changed mitochondria with and without light treatment. This change is likely because the accumulation of DQA in mitochondria interferes with the functioning of membrane proteins and inhibits the mitochondrial respiratory chain.[34] PQC NFs without light treatment were found to cause similar alterations in mitochondria to those observed with DQA, showing that PQC NFs can affect mitochondrial activity. Cells treated with both PQC NFs and light treatment manifested seriously damaged mitochondria, which were indicated by severe cristae disruptions and abnormal vacuoles. In contrast, treatments with PA and light only caused some mitochondrial swelling and the normal mitochondrial microstructures remained intact. Altogether, these findings suggested that PA has very limited effects on mitochondrial photodamage compared to PQC NFs. Due to their mitochondria targeting properties, the light-treated PQC NFs predominantly cause a rapid rise of ROS levels within mitochondria and thus caused mitochondrial imbalance and damage *in situ*. As mitochondria are the indispensable powerhouses of cells, PQC NF-induced mitochondrial damage can be a death blow for cancer cells.

### 2.10. Apoptosis Induction

Decreased mitochondrial membrane potential and subsequent mitochondrial damage are landmark events in the early stages of apoptosis.[35] Hence, we explored the downstream apoptotic effects of mitochondrial damage upon treatment with PQC NFs. The total apoptotic cell population was examined by using double staining with annexin V-APC and propidium iodide (PI). PQC NFs with light generated the highest apoptotic populations among all groups even at a low treated concentration (0.2 μM), while PQC NFs without light did not show proapoptotic effects, suggesting the high phototoxicity and low dark toxicity of PQC NFs (Figure 4e). It should be highlighted that the light-treated control photosensitizer PA failed to induce apoptosis under the same conditions, which can be attributed to its relatively low concentration. When the concentration was increased to 2 μM, the Annexin V positive population of PQC NFs group reached 90.9%, while that of PA was only 19.3% (Figure S15, Supporting information). These results fully reveal the potent pro-apoptotic effect of PQC NFs.

To identify the apoptotic pathways activated by PQC NF-mediated phototherapy, we measured the changes in traditional apoptosis makers through western blot assays.[36] During the process of apoptosis, the cytochrome c sequestered in the intermembrane space

of mitochondria can be released into the cytosol, which leads to the activation of the cytochrome c-dependent caspase cascade.[37] The cytochrome c levels in cells treated with PQC NFs and light were dramatically decreased within mitochondria and increased in the cytoplasm, indicating that PQC NF-induced photodamage could release cytochrome c from mitochondria into the cytosol (Figure 4f). Meanwhile, the downstream apoptotic proteins, including the caspase-3 and its substrate poly (ADP-ribose) polymerase (PARP), were also found cleaved upon the treatment with PQC NFs and light (Figure 4f). Taken together, these results validate that PQC NF-triggered PDT can potentially induce mitochondrial disruption and ultimately cause the apoptosis of cancer cells through the cytochrome c-dependent caspase cascade.

### 2.11. Long-Term Retention in Tumor

As small molecules, the traditional photosensitizers suffer the rapid clearance from tumors.[38] Rapid clearance can result in the low therapeutic concentrations and poor retention of photosensitizers in tumor sites, leading to insufficient therapeutic efficacy and frequent intakes of medicines. Currently, preparing the nanoformulations of a photosensitizer is an effective strategy to overcome these shortcomings in PDT.[9a, 9b] Given their high surface-area-to-volume ratio, the fiber-shaped materials can form strong interactions with biosurface and have enormous potentials to be retained in tumor sites.[39] The oral cancer mouse model was established to verify the corresponding advantages of PQC NFs in tumors because this cancer type is readily accessible to both the illumination with laser, a requirement for effective phototherapy, and the topical (intratumoral) administration of phototherapeutic agents.[40] When PQC NFs were injected intratumorally in nude mice bearing OSC-3 tumors, we found that the PQC NFs exhibited fluorescent signals at the tumor site that persisted for nearly a week longer than free PA (Figure 5a). The fluorescence of PQC NFs within tumors was maintained at a high level for more than ten days, while that of PA was nearly undetectable at the 4th day post-injection, indicating PQC NFs can be retained in tumors for a significant amount of time.

### 2.12. Intratumoral ROS Production

With the advantage of long-term retention, PQC NFs can support multiple light treatments after a single-dose administration. To verify this hypothesis, the light-triggered ROS production in the tumor was monitored at different time points post-injection by using DCF-DA as an indicator.[23, 41] The emission spectra of DCF were not overlapped with that of PQC NFs or PA, indicating that the retained PQC NFs or PA in tumors would not interfere with ROS signals (Figure S16, Supporting information). ROS levels in tumors treated with PA were high at 24 h post-injection and decreased quickly at later time points, while ROS levels in PQC NF-treated tumors were continuously maintained at a high degree during 6 days (Figure 5b and Figure S17, Supporting information). These findings suggest that PQC NFs are very potent photodynamic therapy agents.

### 2.13 In Vivo Antitumor Effect

To evaluate the *in vivo* therapeutic effects of PQC NFs, we established a subcutaneous oral cancer model by implanting OSC-3 cells into the flanks of nude mice to evaluate the phototherapeutic and non-phototherapeutic effects of each drug (Figure 5c). Tumors

on the right side were subjected to laser exposure, while the left side tumors were not. All the mice bearing tumors were randomly assigned into four groups: Vehicle, DQA, PA, and PQC NFs, and were treated according to the treatment schedule shown in Figure 5c. Drug treatment was performed by intratumor injection only once at the beginning of treatments (at Day 0), followed by 4 laser treatments at Day 1, Day 2, Day 5, and Day 6. A low laser power (0.2 W $cm^{-2}$, 6 min) was chosen to minimize the interference from photothermal effects because the phototherapy under this condition did not increase the tumor temperature significantly in both PQC NFs and PA groups (Figure S18, Supporting information). Compared to the vehicle group, the groups without laser (PA, QDA, and PQC NFs) did not show significant antitumor efficacy, suggesting that chemotherapeutic effects of the single-dose drug treatment were very limited (Figure 5d). The groups of vehicle and DQA with laser also did not show an obvious antitumor effect, indicating that laser treatments were not able to interfere with tumor growth in the absence of photosensitizers. The free photosensitizer PA with laser (PA+L) effectively inhibited tumor growth but did not shrink the tumors. Most interestingly, the laser-treated PQC NFs exhibited the best antitumor efficiency, which achieved a 100% complete cure rate.

The orthotopic oral cancer model was also established by implanting OSC-3 cells into the lips of nude mice (Figure 5c). In the orthotopic model, all the tumors were involved in phototherapy with mice being divided into the same drug-treated groups (vehicle, DQA, PA, and PQC NFs) as the subcutaneous model and drug treatment being performed by intratumoral injection on Day 0, followed by 4 laser treatments (Figure 5c). The therapeutic results in the orthotopic model were consistent with those observed in the subcutaneous model, indicating the PQC NFs eliciting a significantly improved phototherapeutic activity over the free photosensitizer PA (Figure 5e). In addition, as shown in Figure 5f, all treatments did not cause a loss in body weight of mice.

The subcutaneous tumors, which were treated with drugs for 24 h, followed by laser treatment or not, were collected for further investigation of tissue-level changes. From TEM, we observed that the laser-activated PQC NFs induced obvious disruption of mitochondrial microstructures of tumors (Figure 5g). Hematoxylin and eosin (H&E) staining results showed that tumor cells were predominantly dying or destroyed in tumors treated with PQC NFs+laser, while only a small portion of tumor tissue showed apoptosis/necrosis in the PA with laser group (Figure 5h). The nuclei were intact and showed bright blue staining in both vehicle and DQA groups, indicating no significant cell death occurred in these groups. Immunohistochemical (IHC) analysis against Ki67 demonstrated that cell proliferation in the laser-treated PQC NFs group was significantly suppressed compared to all other groups (Figure 5i). In the H&E staining results of normal organs (Figure S19, Supporting information), there were no obvious changes of their physiological morphology found among the groups, indicating the relatively high safety of PQC NFs. These *in vivo* therapeutic results fully demonstrated that PQC NFs are promising agents to improve photodynamic cancer therapy.

## 3. Conclusion

In summary, according to the strategies of photosensitizer improvement and the principles of new drug design and molecular self-assembly, we developed a new mitochondria-targeting small-molecule photosensitizer that can self-assemble into nanofibers (PQC NFs). By targeting and disrupting mitochondria, the phototherapy mediated by PQC NFs induced significant apoptosis and exhibited nanomolar cytotoxicity. This targeting approach overcomes insufficient potency of traditional photosensitizers as anticancer therapies. Hence, PQC NFs showed significantly improved in vitro anticancer potency compared to both free and nanoformulated PA. Additionally, as nanoscale materials, PQC NFs also demonstrated long-term retention in tumor sites, solving the challenge of rapid clearance from tumors found in existing small-molecule photosensitizers. With these advantages, PQC NFs achieved a significant antitumor effect *in vivo* by affording a 100% complete cure rate on both subcutaneous and orthotopic oral cancer models with only a single-dose administration.

In contrast to the conventional nanoformulations that are prepared by physical loading or prodrug self-assembly of existing drugs, PQC NFs are formed by the self-assembly of one-component new chemical entities, which not only represent a structural innovation in the perspective of new drug discovery but also show enormous potentials to break through the drug-loading and scale-up production limitations of the conventional drug delivery systems. Furthermore, PQC NFs also have the unique fiber-shaped nanostructure that is rarely found among the existing small-molecule nanomaterials because the majority of developed nanofibers are based on the peptides with a specific sequence. To the best of our knowledge, PQC NFs represent the first example of single small molecule-assembled nanophotosensitizers, which refer to a transdisciplinary design strategy to advance the phototherapeutic efficiency of traditional photosensitizers from both perspectives of molecule design and nanoformulation.

## 4. Experimental Section

### Preparation and Characterization of PQC NFs:

Briefly, PQC monomers in ethanol were added dropwise into deionized water under stirring. Ethanol in the solution was removed by vacuum rotary evaporation at 37 °C and the self-assembling PQC NFs were formed spontaneously. The aqueous nanofiber solution (0.02 mg $mL^{-1}$) was deposited on copper grids to prepare samples for transmission electron microscope (TEM). The morphology was observed by a Talos L120C TEM (Thermo Fisher Scientific, USA). The UV-Vis and fluorescence spectra were measured by a UV-Vis spectrometer (UV-1800, Shimadzu, Japan) and a fluorescence spectrometer (RF-6000, Shimadzu, Japan), respectively. NIR fluorescence imaging studies was performed by a ChemiDoc™ MP imaging system (Bio-Rad, USA). The $^1O_2$ production was detected using SOSG (Thermo Fisher Scientific, USA) as an indicator. Briefly, SOSG solution was added into drug solutions in 96 wells plate. The mixed solutions containing 0.25% SDS (w/v) or not were then irradiated for 60 s using a 633-nm LED array (Omnilux new-U, PhotoTherapeutics, USA) at a power density of 30 mW $cm^{-2}$ at room temperature. Fluorescence intensity was determined by a microplate reader (Tecan, Switzerland). The

ultrafiltration experiment of PQC NFs were conducted using a centrifuge (10k rpm, 10 min) and a centrifuge tube (10 kDa, Beckman Coulter, USA).

### Cell Viability Assay:

OSC-3, BXPC-3, AsPC-1, PANC-1, UM-UC-3, 5637, or IMR90 cells were seeded in 96-well plates at a density of $5\times10^3$ cells per well and were grown overnight. Cells were incubated with various concentrations of drugs for 24 h, followed washing with PBS three times, and adding 100 μL fresh medium. For light-treated groups, cells were irradiated for 30 s using a 633-nm LED array (Omnilux new-U) at a power density of 30 mW $cm^{-2}$ at room temperature and then were cultured for another 24 h in parallel with non-light treated groups. Cell viability was quantified using the CellTiter-Glo assay (Promega, USA).

### Cellular Uptake Assay:

OSC-3 were seeded in 96-well plate at a density of $5\times10^3$ cells per well and grown overnight. PA and PQC NFs (1 μM) were added at predetermined time points. At the end, cells were lysed for 15 min with DMSO solution containing 0.5% Triton x-100. Fluorescence intensity (Ex=412 nm, Em=675 nm) was measured by a microplate reader (Tecan, Switzerland).

### Endocytosis Pathway Study:

OSC-3 cells were seeded in 6-well plate ($3\times10^5$ cells per well) and were grown overnight. Cells were subjected to various treatments as follow: (1) 30 min incubation at either 4 °C or 37 °C; (2) 60 min incubation with endocytosis inhibitors: sodium azide (1 mg $mL^{-1}$, Sigma-Aldrich), chlorpromazine (20 μg $mL^{-1}$, Sigma-Aldrich), genistein (10 μg $mL^{-1}$, Combi-Blocks) and amiloride (50 μM, Alfa Aesar). Cells were then treated with PQC NFs (1 μM) for 2 h. After washed three times with cold PBS, cells were lysed for 15 min with DMSO solution containing 0.5% Triton x-100. Fluorescence intensity (Ex=412 nm, Em=675 nm) was measured by a microplate reader (Tecan, Switzerland).

### Colocalization Assay:

OSC-3 cells were treated with PQC NFs (2 μM) for various times (from 5 min to 8 h) or with PA (2 μM) for 4 h, followed by incubation with LysoTracker Green (Thermo Fisher Scientific, USA) and MitoTracker Red (Cell Signaling Technology, USA) for 30 min. Cells were visualized on confocal laser scanning microscopy (CLSM) (Carl Zeiss, Germany) immediately to investigate the subcellular localization. Signals of PQC NPs and PA were observed on the Cy5 channel. LysoTracker and MitoTracker were observed according the manufacturer's instructions. The corresponding Pearson correlation coefficient was calculated by ImageJ software.

### Isolation of Mitochondrial, Lysosomal, and Cytoplasmic Fractions:

$2\times10^7$ OSC-3 cells were seeded into a 150 mm cell culture dishes and grown overnight. Cells were treated for 24 h with PQC NFs or PA (1 μM), respectively. After washing with PBS three times, the mitochondrial and cytoplasmic fractions were isolated using a mitochondria isolation kit (Thermo Fisher Scientific, USA), or the lysosomes were isolated

using a lysosome Enrichment Kit (Thermo Fisher Scientific, USA). Fluorescence intensity of the mitochondrial and cytoplasm fractions were determined by a microplate reader (Tecan, Switzerland). Data were normalized by per μg protein.

### Measurement of Intracellular ROS Production:

OSC-3 cells were seeded in 6-well plates at a density of $5\times10^5$ cells per well and were grown overnight. Cells were then were treated with PA and PQC NFs (1 μM) for 24 h. After washed three times with PBS, cells were incubated with 10 μM of 2',7'-dichlorofluorescein diacetate (DCF-DA) (Sigma-Aldrich, USA) for 20 min, followed by another three times washing procedure with PBS. Cells were irradiated for 30 s using a 633-nm LED array (Omnilux new-U) at a power density of 30 mW $cm^{-2}$ at room temperature and then were cultured for 30 min. Cells were collected and analyzed by a BD FACSCanto flow cytometer (BD, USA).

### Mitochondrial Membrane Potential Assay:

The mitochondrial membrane potential was determined using the dye JC-1 as a probe (Thermo Fisher Scientific, USA). Briefly, OSC-3 cells ($2\times10^4$ cells per well) were treated with drugs (1 μM) for 24 h. After washing three times with PBS and adding 100 μL fresh medium, cells were irradiated for 30 s using a 633-nm LED array (Omnilux new-U) at a power density of 30 mW $cm^{-2}$ at room temperature and were cultured for another 2 h. JC-1 (5 μg $mL^{-1}$) was added to incubate for 20 min. Cell imaging was performed on a CLSM (Carl Zeiss, Germany). The ratio of red/green fluorescence intensity was calculated by ImageJ software.

### Apoptosis Assay:

Apoptosis assay was performed with the Annexin V-APC/propidium iodide (PI) apoptosis kit (Biolegend, USA). Briefly, OSC-3 cells ($5\times10^5$ cells per well) were treated with different drugs (0.2 μM) for 24 h. After washing three times with PBS and adding 100 μL fresh medium, cells were irradiated for 30 s using a 633-nm LED array (Omnilux new-U) at a power density of 30 mW $cm^{-2}$ at room temperature, and were cultured for another 12 h. Cells were stained with the apoptosis kit according to the manufacturer's instructions. All samples of cells were collected for flow cytometry using a BD FACSCanto flow cytometer (BD, USA). Data analysis was accomplished using FlowJo software.

### Western Blot Analysis:

OSC-3 cells were treated with PQC NFs (0.5 μM) for 24 h, followed by washing three times with PBS and treatment with or without light (30 mW $cm^{-2}$) for 30 s. Cells were cultured for another 24 h, and then the mitochondrial and the cytoplasmic proteins were isolated using a mitochondria isolation kit (Thermo Fisher Scientific, USA). Proteins were quantified using a BCA protein assay kit (Thermo Fisher Scientific, USA), then separated on 12% SDS-polyacrylamide gel electrophoresis (PAGE), and finally transferred onto polyvinylidene difluoride (PVDF) membranes (Millipore Sigma, USA). The membrane was blocked by 5% non-fat milk for 1 h and then incubated with the primary antibodies at 4 °C overnight. After subsequent washing with tris-buffered saline with 0.1% Tween 20 (TBST), the

membrane was incubated with the secondary antibody for 1 h at room temperature. The immunoreactive bands were detected using the enhanced chemiluminescence detection kit (ProtoGlow ECL, National Diagnostics, USA) and imaged by the ChemiDoc™ MP imaging system (Bio-Rad, USA). Antibodies were used as followed: cytochrome C, caspase-3, cleaved caspase-3, PARP, and β-actin. All antibodies were from Cell Signaling Technology (USA).

### Cell and Tissue TEM Study:

OSC-3 cells (20k per well) in an 8-well slide plate (Thermo Fisher Scientific, USA) were incubated with drugs (0.5 μM) for 24 h, then were washed with PBS three times, and were treated with or without light for 30 s. After another 2 h incubation, cells were fixed with the 0.1 M cacodylate buffer containing 2.5% glutaraldehyde plus 2% paraformaldehyde, and transferred to the carbon square mesh, followed by observation using a Talos L120C TEM (Thermo Fisher Scientific, USA). In the investigation of intracellular dissociation, PQC NFs (100 μM) were incubated with the freshly isolated mitochondria (0.1 mg $mL^{-1}$), lysosomes (0.1 mg $mL^{-1}$), and other cellular components (0.1 mg $mL^{-1}$) for 24 h and were then observed by the same TEM as mentioned above.

### Animal Models:

Female athymic nude mice, 6-week-old, were purchased from Envigo (Indianapolis, IN, USA). All animal experiments were strictly performed in compliance with the protocol (#20265) approved by the Institutional Animal Care and Use Committee at the University of California, Davis. The subcutaneous and orthotopic tumor models were established by inoculated OSC-3 cells into both flanks ($5\times10^6$ cells per tumor) or lower lips ($1\times10^6$ cells per tumor) of nude mice. When the subcutaneous tumors reached about 80 $mm^3$ and orthotopic tumors reached about 50 $mm^3$, the mice started to be treated as indicated.

### In Vivo Imaging Study:

The subcutaneous tumor model was used in fluorescence imaging study *in vivo* of PA and PQC NFs. PA and PQC NFs (10 nmol per 50 $mm^3$ tumor) were administered by intratumoral injection. Fluorescence imaging were performed on a ChemiDoc™ MP imaging system (Bio-Rad, USA) at different time points post-injection.

### In Vivo Anticancer Study:

Laser (680 nm) treatment was conduct by a laser device within an energy of 0.2 W $cm^{-2}$ for 6 min (Shanghai Xilong Optoelectronics Technology, China). Mice bearing subcutaneous and orthotopic tumors were randomly divided into four groups (n=6): Vehicle (PBS), DQA, PA, and PQC NFs. The drug was intratumorally injected into mice at a dose of 1mM (10 nmol per 50 $mm^3$ tumor). Laser treatment was performed for a total of four times, one each on days 1, 2, 5, and 6 post-injection of drugs. The relative tumor value and body weight were recorded every two days. In subcutaneous models, the tumors in the right flank of mice were subjected to laser treatment, while the left tumors were not. In orthotopic models, all tumors were treated with the laser treatment. The temperature of tumor surface was monitored using a thermal camera (FLIR Systems, USA) immediately after laser treatment.

ROS production in the tumor after light treatment was also measured using DCF-DA as an indicator. ROS production in the tumor after light treatment was also measured using DCF-DA as an indicator. Briefly, the tumor was treated with different drugs via intratumoral injection at first. Then, the mice with tumors were treated with the laser at 1st, 2nd, 5th, and 6th day independently. After each light treatment, the mice were sacrificed immediately, and the obtained tumors were cut into small pieces and immersed in the DCF-DA solutions for 10 min. Finally, the tumors pieces were imaged by the ChemiDoc™ MP imaging system with the FITC channel. The fluorescence intensity of DCF-DA was quantified by Image J software. Mice were sacrificed after the first light treatment to obtain tumor and organs tissue for TEM, H&E, and IHC evaluation.

## Supplementary Material

Refer to Web version on PubMed Central for supplementary material.

## Acknowledgments

We thank the support from NIH/NCI (R01CA199668, R01CA232845), NIH/NIDCR (R01DE029237), NIH/NICHD (R01HD086195), and UC Davis Comprehensive Cancer Center Support Grant (CCSG) awarded by the National Cancer Institute (NCI P30CA093373). The authors also appreciate the access to the Molecular Pharmacology Shared Resources funded by the CCSG.

## References

[1]. Dolmans DEJGJ, Fukumura D, Jain RK, Nat. Cell. Biol 2003, 3, 380.

[2]. Civantos FJ, Karakullukcu B, Biel M, Silver CE, Rinaldo A, Saba NF, Takes RP, Vander Poorten V, Ferlito A, Adv. Ther 2018, 35, 324. [PubMed: 29417455]

[3]. a)MESQUITA MQ, DIAS CJ, GAMELAS S, FARDILHA M, NEVES MGPMS, FAUSTINO MAF, An. Acad. Bras. Cienc 2018, 90, 1101; [PubMed: 29873674] b)Xiao Q, Lin H, Wu J, Pang X, Zhou Q, Jiang Y, Wang P, Leung W, Lee H, Jiang S, Yao SQ, Gao L, Liu G, Xu C, J. Med. Chem 2020, 63, 4896. [PubMed: 32267685]

[4]. a)Mahalingam SM, Ordaz JD, Low PS, ACS Omega 2018, 3, 6066; [PubMed: 30023938] b)Zhao X, Yang Y, Yu Y, Guo S, Wang W, Zhu S, Chem. Commun 2019, 55, 13542.

[5]. a)Verma S, Watt GM, Mai Z, Hasan T, Photochem. Photobiol 2007, 83, 996; [PubMed: 17880492] b)Jeena MT, Palanikumar L, Go EM, Kim I, Kang MG, Lee S, Park S, Choi H, Kim C, Jin S-M, Bae SC, Rhee HW, Lee E, Kwak SK, Ryu J-H, Nat. Commun 2017, 8, 26; [PubMed: 28638095] c)Cheng G, Zhang Q, Pan J, Lee Y, Ouari O, Hardy M, Zielonka M, Myers CR, Zielonka J, Weh K, Chang AC, Chen G, Kresty L, Kalyanaraman B, You M, Nat. Commun 2019, 10, 2205. [PubMed: 31101821]

[6]. a)Noh I, Lee D, Kim H, Jeong C-U, Lee Y, Ahn J-O, Hyun H, Park J-H, Kim Y-C, Adv. Sci 2018, 5, 1700481;b)Chakrabortty S, Agrawalla BK, Stumper A, Vegi NM, Fischer S, Reichardt C, Kögler M, Dietzek B, Feuring-Buske M, Buske C, Rau S, Weil T, J. Am. Chem. Soc 2017, 139, 2512; [PubMed: 28097863] c)Jean SR, Ahmed M, Lei EK, Wisnovsky SP, Kelley SO, Acc. Chem. Res 2016, 49, 1893; [PubMed: 27529125] d)Zorova LD, Popkov VA, Plotnikov EY, Silachev DN, Pevzner IB, Jankauskas SS, Babenko VA, Zorov SD, Balakireva AV, Juhaszova M, Sollott SJ, Zorov DB, Anal. Biochem 2018, 552, 50; [PubMed: 28711444] e)Chen W-H, Luo G-F, Zhang X-Z, Adv. Mater. 2019, 31, 1802725.

[7]. a)Solban N, Rizvi I, Hasan T, Laser Surg. Med 2006, 38, 522;b)Zhang C-J, Hu Q, Feng G, Zhang R, Yuan Y, Lu X, Liu B, Chemical Science 2015, 6, 4580; [PubMed: 28717475] c)Gao Y, Shi J, Yuan D, Xu B, Nat. Commun 2012, 3, 1033. [PubMed: 22929790]

[8]. Busch T, Hahn SM, Cancer Biol. Ther 2005, 4, 203.

[9]. a)Lismont M, Dreesen L, Wuttke S, Adv. Funct. Mater. 2017, 27, 1606314;b)Lucky SS, Soo KC, Zhang Y, Chem. Rev 2015, 115, 1990; [PubMed: 25602130] c)Krogstad EA, Ramanathan R, Nhan C, Kraft JC, Blakney AK, Cao S, Ho RJY, Woodrow KA, Biomaterials 2017, 144, 1; [PubMed: 28802690] d)Yoo JJ, Kim C, Chung C-W, Jeong Y-I, Kang DH, Int. J. Nanomedicine 2012, 7, 1997; [PubMed: 22619537] e)Zhao F, Ma ML, Xu B, Chem. Soc. Rev 2009, 38, 883. [PubMed: 19421568]

[10]. a)Ma Z, Li J, Lin K, Ramachandran M, Zhang D, Showalter M, De Souza C, Lindstrom A, Solano LN, Jia B, Urayama S, Duan Y, Fiehn O, Lin T.-y, Li M, Li Y, Nat. Commun 2020, 11, 4615; [PubMed: 32934241] b)Yang X, Ma C, Chen Z, Liu J, Liu F, Xie R, Zhao H, Deng G, Chen AT, Gong N, Yao L, Zuo P, Zhi K, Wang J, Gao X, Wang J, Fan L, Zhou J, Nano Res. 2019, 12, 2468; [PubMed: 35966168] c)Xing P, Zhao Y, Adv. Mater. 2016, 28, 7304; [PubMed: 27273862] d)Ma W, Cheetham AG, Cui H, Nano Today 2016, 11, 13. [PubMed: 27066106]

[11]. a)Cheng L, Wang C, Feng L, Yang K, Liu Z, Chem. Rev 2014, 114, 10869; [PubMed: 25260098] b)Cheng G, Wang H, Zhang C, Hao Y, Wang T, Zhang Y, Tian Y, Chang J, Chem. Eng 2020, 390, 124447.

[12]. a)Dhand C, Dwivedi N, Sriram H, Bairagi S, Rana D, Lakshminarayanan R, Ramalingam M, Ramakrishna S, in Nanofiber Composites for Biomedical Applications, (Eds: Ramalingam M, Ramakrishna S.), Woodhead Publishing 2017, p. 199;b)Prabhu P, in Handbook of Nanofibers, DOI: 10.1007/978-3-319-53655-2_48 (Eds: Barhoum A, Bechelany M, Makhlouf ASH), Springer International Publishing, Cham 2019, p. 831;c)Zupančič Š, Sinha-Ray S, Sinha-Ray S, Kristl J, Yarin AL, Mol. Pharm 2016, 13, 295. [PubMed: 26635214]

[13]. a)Moore AN, Hartgerink JD, Acc. Chem. Res 2017, 50, 714; [PubMed: 28191928] b)Cheetham AG, Zhang P, Lin Y.-a, Lock LL, Cui H, J. Am. Chem. Soc 2013, 135, 2907. [PubMed: 23379791]

[14]. Sis MJ, Webber MJ, Trends Pharmacol. Sci 2019, 40, 747. [PubMed: 31493931]

[15]. Sun Z, Li Z, He Y, Shen R, Deng L, Yang M, Liang Y, Zhang Y, J. Am. Chem. Soc 2013, 135, 13379. [PubMed: 23984683]

[16]. a)Wang Z, Guo W, Kuang X, Hou S, Liu H, Asian J. Pharm. Sci 2017, 12, 498;b)Teguh SC, Klonis N, Duffy S, Lucantoni L, Avery VM, Hutton CA, Baell JB, Tilley L, J. Med. Chem 2013, 56, 6200; [PubMed: 23837878] c)Pathak RK, Kolishetti N, Dhar S, WIREs Nanomed. Nanobiotechnol 2015, 7, 315.

[17]. Liang C, Zhang L, Zhao W, Xu L, Chen Y, Long J, Wang F, Wang L, Yang Z, Adv. Healthc. Mater. 2018, 7, 1800899.

[18]. a)Lombardo D, Kiselev MA, Magazù S, Calandra P, Advances in Condensed Matter Physics 2015, 2015;b)Shimizu T, Masuda M, Minamikawa H, Chemical Reviews 2005, 105, 1401. [PubMed: 15826016]

[19]. Li L-L, Ma H-L, Qi G-B, Zhang D, Yu F, Hu Z, Wang H, Adv. Mater. 2016, 28, 254. [PubMed: 26568542]

[20]. a)Young LM, Saunders JC, Mahood RA, Revill CH, Foster RJ, Tu L-H, Raleigh DP, Radford SE, Ashcroft AE, Nat. Chem 2015, 7, 73; [PubMed: 25515893] b)Zheng J, Fan R, Wu H, Yao H, Yan Y, Liu J, Ran L, Sun Z, Yi L, Dang L, Gan P, Zheng P, Yang T, Zhang Y, Tang T, Wang Y, Nat. Commun 2019, 10, 1604. [PubMed: 30962431]

[21]. a)Weissig V, Lasch J, Erdos G, Meyer HW, Rowe TC, Hughes J, Pharm. Res 1998, 15, 334; [PubMed: 9523323] b)Weissig V, Pharmaceutical Research 2011, 28, 2657. [PubMed: 21833792]

[22]. Qin SY, Zhang AQ, Cheng SX, Rong L, Zhang XZ, Biomaterials 2017, 112, 234. [PubMed: 27768976]

[23]. Li Y, Lin T.-y., Luo Y, Liu Q, Xiao W, Guo W, Lac D, Zhang H, Feng C, Wachsmann-Hogiu S, Walton JH, Cherry SR, Rowland DJ, Kukis D, Pan C, Lam KS, Nat. Commun 2014, 5, 4712. [PubMed: 25158161]

[24]. Zhou Y, Liang X, Dai Z, Nanoscale 2016, 8, 12394. [PubMed: 26730838]

[25]. Zhou L, Wu Y, Meng X, Li S, Zhang J, Gong P, Zhang P, Jiang T, Deng G, Li W, Sun Z, Cai L, Small 2018, 14, 1801008.

[26]. a)Zhang Y, Bo S, Feng T, Qin X, Wan Y, Jiang S, Li C, Lin J, Wang T, Zhou X, Jiang Z-X, Huang P, Adv. Mater. 2019, 31, 1806444;b)Ng KK, Lovell JF, Vedadi A, Hajian T, Zheng G, ACS Nano 2013, 7, 3484. [PubMed: 23464857]

[27]. Mimikos C, Shafirstein G, Arshad H, World J. Otorhinolaryngol. Head Neck Surg 2016, 2, 126.

[28]. a)Ji Y, Xiao Y, Xu L, He J, Qian C, Li W, Wu L, Chen R, Wang J, Hu R, Zhang X, Gu Z, Chen Z, Advanced Science 2018, 5, 1700867;b)Mosquera J, García I, Liz-Marzán LM, Accounts of Chemical Research 2018, 51, 2305; [PubMed: 30156826] c)Behzadi S, Serpooshan V, Tao W, Hamaly MA, Alkawareek MY, Dreaden EC, Brown D, Alkilany AM, Farokhzad OC, Mahmoudi M, Chem. Soc. Rev 2017, 46, 4218. [PubMed: 28585944]

[29]. Jakka SR, Govindaraj V, Mugesh G, Angew Chem. Int. Ed 2019, 58, 7713.

[30]. a)Chen R, Wang J, Qian C, Ji Y, Zhu C, Wu L, Li W, Bi X, Wang Y, Cao G, Chen Z, Adv. Funct. Mater. 2019, 29, 1806058;b)Ding L, Yao C, Yin X, Li C, Huang Y, Wu M, Wang B, Guo X, Wang Y, Wu M, Small 2018, 14, 1801451.

[31]. Agostinis P, Berg K, Cengel KA, Foster TH, Girotti AW, Gollnick SO, Hahn SM, Hamblin MR, Juzeniene A, Kessel D, Korbelik M, Moan J, Mroz P, Nowis D, Piette J, Wilson BC, Golab J, CA Cancer J Clin. 2011, 61, 250. [PubMed: 21617154]

[32]. Zorov DB, Juhaszova M, Sollott SJ, Physiol. Rev 2014, 94, 909. [PubMed: 24987008]

[33]. Zhang W, Hu X, Shen Q, Xing D, Nat. Commun 2019, 10, 1704. [PubMed: 30979885]

[34]. Belosludtsev KN, Belosludtseva NV, Tenkov KS, Sharapov VA, Kosareva EA, Dubinin MV, Biochem. (Mosc) Suppl. Ser. A Membr. Cell Biol 2018, 12, 121.

[35]. Lakhani SA, Masud A, Kuida K, Porter GA, Booth CJ, Mehal WZ, Inayat I, Flavell RA, Science 2006, 311, 847. [PubMed: 16469926]

[36]. Li Y, Tan C-P, Zhang W, He L, Ji L-N, Mao Z-W, Biomaterials 2015, 39, 95. [PubMed: 25477176]

[37]. a)Martinou J-C, Desagher S, Antonsson B, Nat. Cell Biol 2000, 2, E41; [PubMed: 10707095] b)Waterhouse NJ, Trapani JA, Cell Death Differ. 2003, 10, 853. [PubMed: 12815469]

[38]. Shirasu N, Nam SO, Kuroki M, Anticancer Res. 2013, 33, 2823. [PubMed: 23780966]

[39]. Spela Z, Petra K, Sasa B, Julijana K, Curr. Pharm. Des 2015, 21, 3257. [PubMed: 26027560]

[40]. Van Straten D, Mashayekhi V, De Bruijn HS, Oliveira S, Robinson DJ, Cancers 2017, 9, 19. [PubMed: 28218708]

[41]. a)Lee W-J, Hsiao M, Chang J-L, Yang S-F, Tseng T-H, Cheng C-W, Chow J-M, Lin K-H, Lin Y-W, Liu C-C, Lee L-M, Chien M-H, Arch. Toxicol 2015, 89, 1103; [PubMed: 25138434] b)Zhang Y, Zhang L, Wang Z, Wang F, Kang L, Cao F, Dong K, Ren J, Qu X, Biomaterials 2019, 223, 119462.

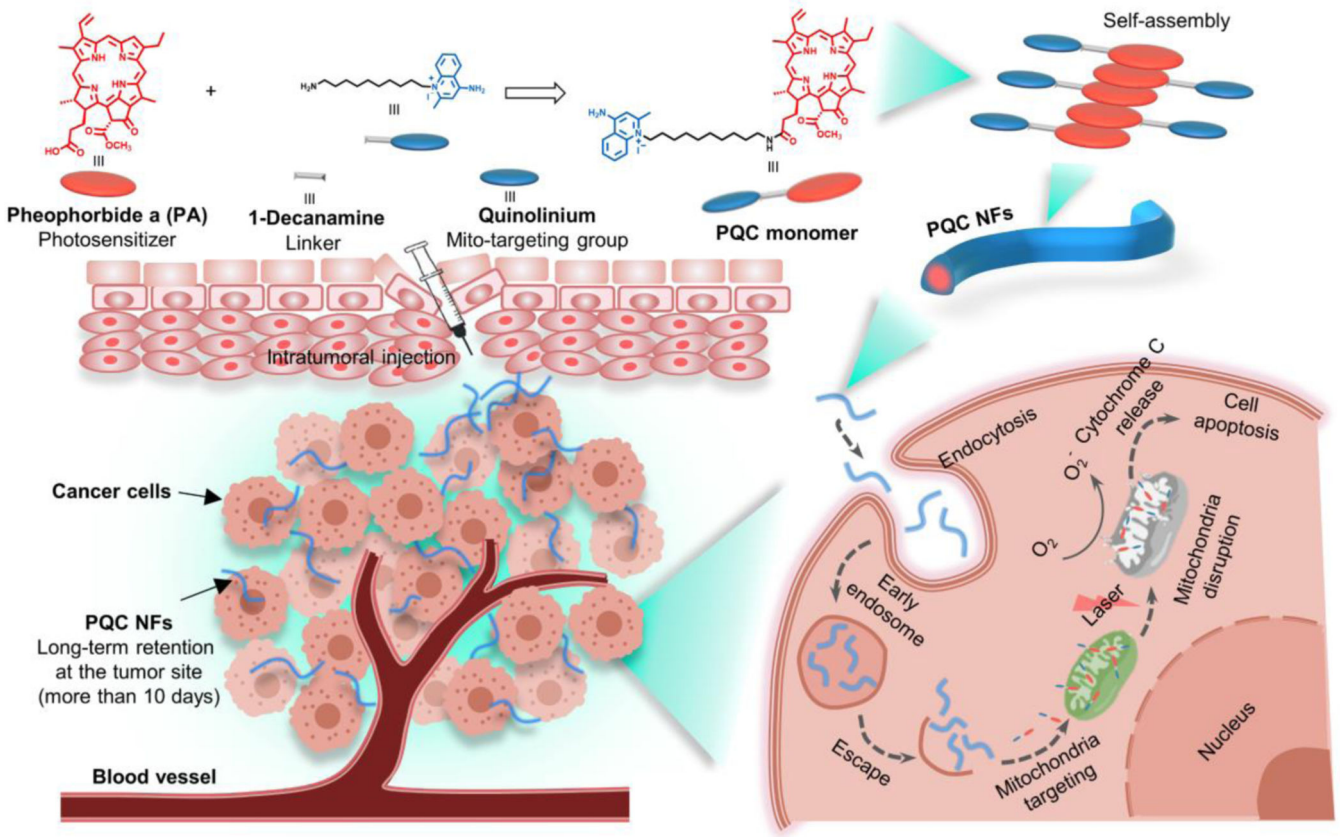


**Figure 1.**

Schematic illustration of single small molecule-assembled mitochondria targeting nanofibers (PQC NFs). The PQC monomer is a conjugate of pheophorbide a (PA) and quinolinium. PQC NFs exhibited nanomolar cytotoxicity by mediating mitochondria-targeting phototherapy and were retained long-term at the tumor site. With these advantages, PQC NFs achieved robust anticancer effects *in vivo* with a 100% complete cure rate after the administration of only a single dose.

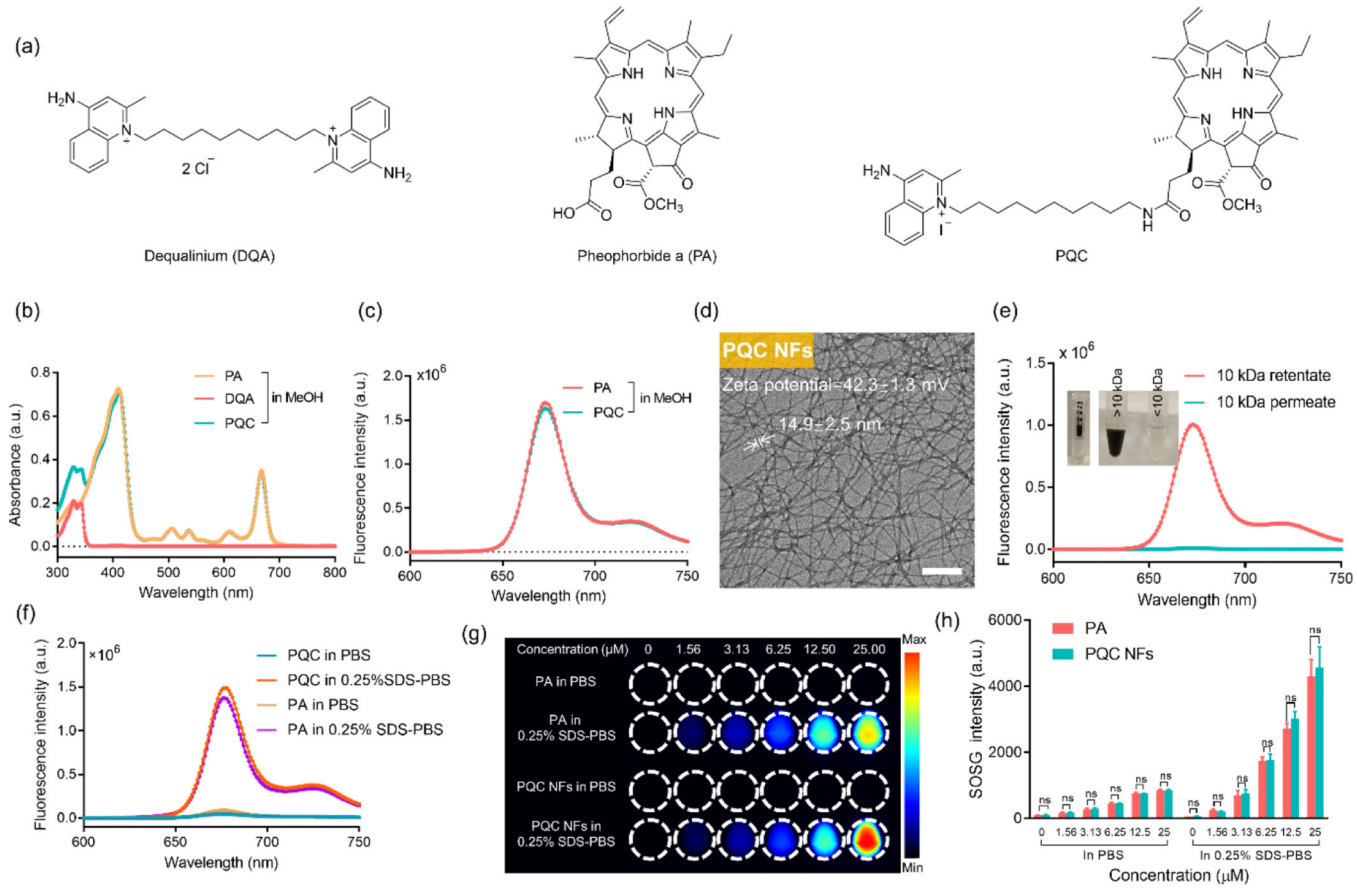


**Figure 2.**

(a) Chemical structures of DQA, PA and PQC. (b) Absorbance spectra of DQA (5 μM), PA (10 μM), and PQC (10 μM) in methanol. (c) Fluorescent spectra of PA and PQC (10 μM) in methanol (λex=412 nm). (d) Transmission electron microscope (TEM) photograph of PQC NFs. Scale bar=200 nm. (e) Appearance and fluorescence spectra of PQC NFs after centrifugal filtration (10 kDa). The working concentration is 2 mM for centrifugation, and the spectra were measured after dilution with methanol (1:500). (f) Fluorescence spectra of PQC NFs or PA (20 μM) in the assembly (PBS) and dissociation (PBS/SDS) forms. (g) Fluorescence imaging under Cy5 channel of PQC NFs or PA in the assembly (PBS) and dissociation (PBS/SDS) forms. (h) Singlet oxygen production of PA and PQC NFs measured by using SOSG as an indicator. The solutions of PA and PQC NFs in PBS and PBS/SDS were exposed to the NIR light (30 mW $cm^{-2}$) for 60 s.

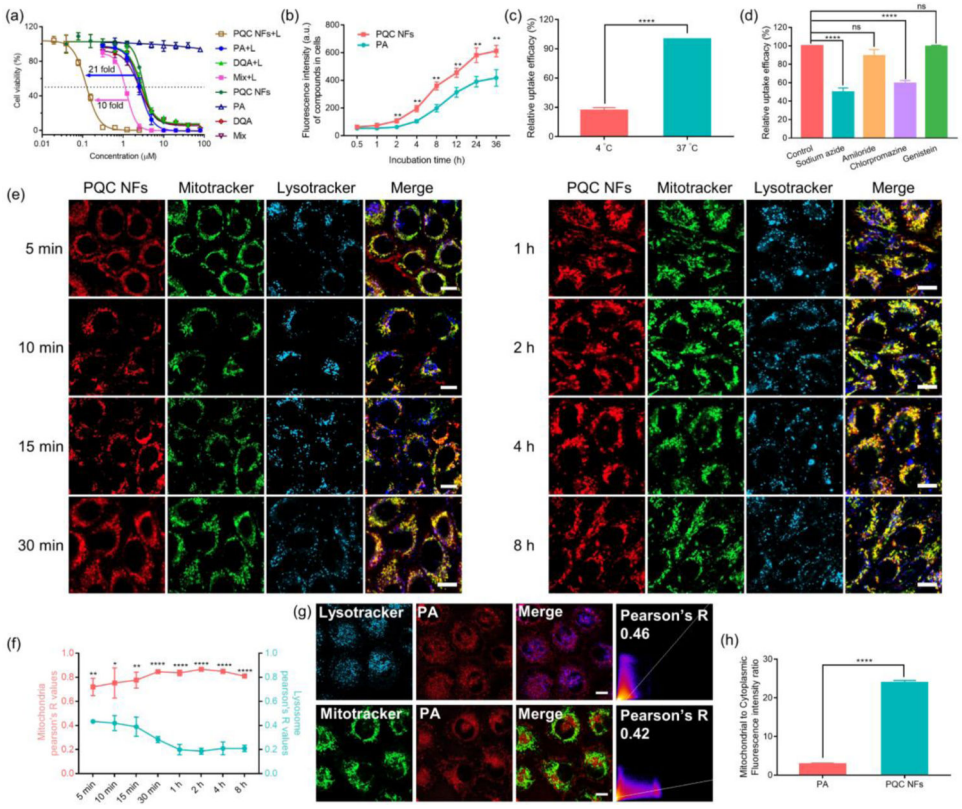


**Figure 3.**

(a) Cell viability. OSC-3 cells were incubated as indicated for 24 h and then were treated with or without light treatment (30 mW $cm^{-2}$ for 30 s), followed by another 24 h incubation. (b) Time-course of cellular uptake for PA and PQC NFs (1 μM) in OSC-3 cells. (c, d) Influence of temperature (c) and various inhibitors (d) on the endocytosis of PQC NFs. (e) Representative fluorescence images of the time-dependent localization for PQC NFs (2 μM) in OSC-3 cells. Scale bar=10 μm. Images were captured under the condition of the best signal for the accurate colocalization analysis, therefore, the brightness did not represent the relative fluorescence intensity of individual images. (f) Calculated Pearson correlation coefficient (Pearson's R) for colocalization analysis of images in (e). (g) Cellular distribution of free PA. OSC-3 cells were incubated with PA (2 μM) for 4 h. Scale bar=10 μm. (h) Fluorescence ratio of PA or PQC in mitochondria and cytoplasm. Mitochondria and cytoplasm fractions were isolated from OSC-3 cells that were pretreated with PA and PQC NFs (1 μM) for 24 h.

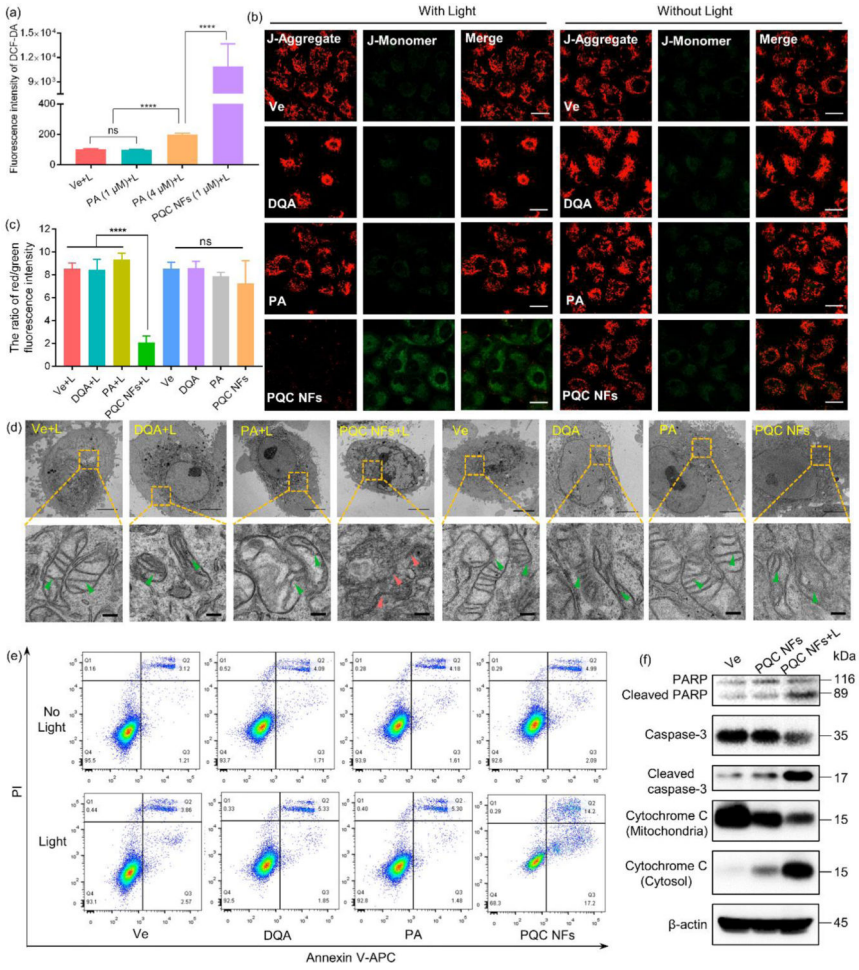


**Figure 4.**

(a) Flow cytometry analysis of ROS levels in OSC-3 cells using DCF-DA as an indicator. (b) Mitochondrial membrane potential analysis of OSC-3 cells that were treated as indicated (1 μM) and stained with JC-1. (c) Quantitative red to green fluorescence ratio of cells in (b). (d) Representative TEM graphs showing morphological changes of mitochondria in OSC-3 cells that were treated as indicated (0.5 μM, 24 h). The green and red arrows designate the normal and damaged mitochondria, respectively. Scale bars are 5 μm (upper panel) and 200 nm (lower panel). (e) Apoptosis assay of OSC-3 cells within the indicated treatments (0.2 μM). (f) Changes of apoptosis-related proteins, including cytochrome C, PARP, and caspase 3, in OSC-3 cells that were treated with PQC NFs (0.5 μM) with or without light. The above-mentioned light treatment was performed for 30 s using a 633-nm LED array at a power density of 30 mW $cm^{-2}$ at room temperature.

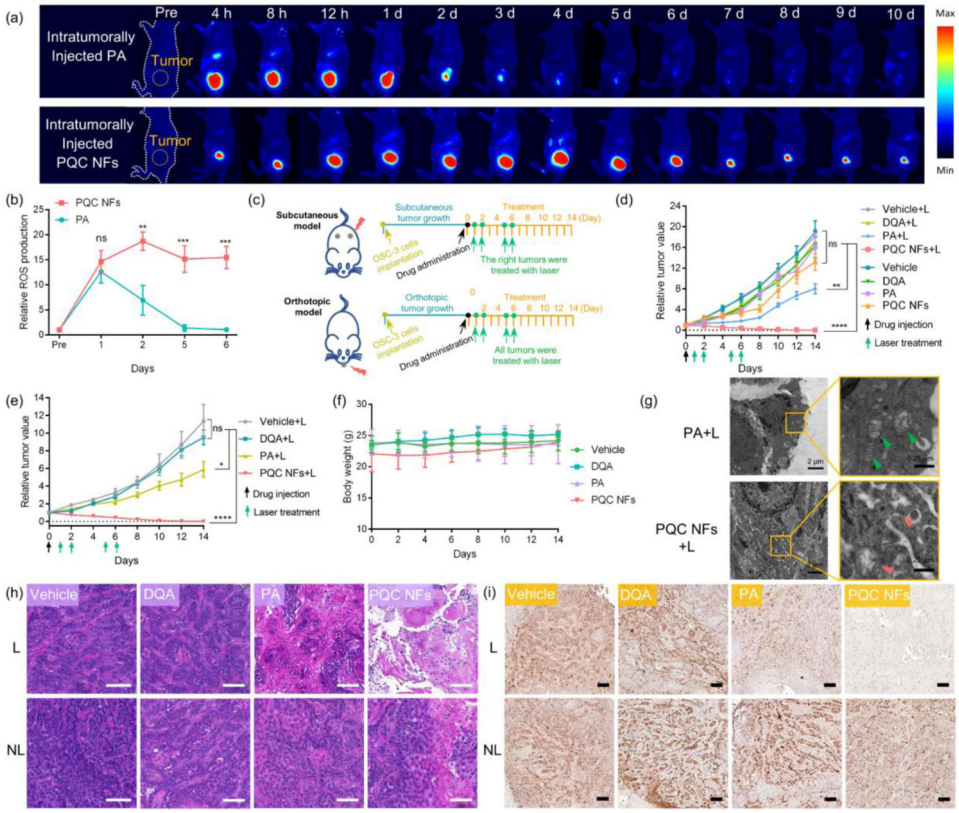


**Figure 5.**

(a) Time-course *in vivo* fluorescence imaging of mice bearing the subcutaneous OSC-3 tumor. Mice were treated with PA or PQC NFs via intratumoral injection (10 nmol per 50 $mm^3$) and were observed at the indicated time points. (b) Intratumoral ROS levels that were measured by *ex vivo* imaging at different intervals post-injection of PA or PQC NFs, in which DCF-DA was used as an indicator. (c) The establishment of subcutaneous (up) and orthotopic (down) oral tumor models, and the treatment schedules. Drugs (10 nmol per 50 $mm^3$) were injected intratumorally at Day 0. The subcutaneous tumors in right flank and the orthotopic tumors were then treated with laser on Day 1, Day 2, Day 5, and Day 6. The laser (680 nm) doses were all set as 0.2 W $cm^{-2}$ for 6 min. (d) Tumor growth curves for the subcutaneous tumor model (n=6). (e) Tumor growth curves for the orthotopic tumor model (n=6). The relative tumor volume is the ratio of the absolute volume of the respective tumor on day x to the absolute volume of the same tumor on day 0. (f) Body weight changes of mice (n=6) for the orthotopic tumor model. (g) Representative TEM graphs of subcutaneous tumors that were treated with PA or PQC NFs for 24 h, followed with laser treatment. The green and red arrows designate the normal and damaged mitochondria, respectively. (h, i) Representative results of H&E (h) and Ki67-IHC. (i) Staining analysis of subcutaneous tumors that were treated with PA or PQC NFs for 24 h, followed by laser treatment or not. Scale bar=100 μm.